

Article

# Response of Coastal Water in the Taiwan Strait to Typhoon Nesat of 2017

Renhao Wu <sup>1,2</sup> , Qinghua Yang <sup>1,3</sup> , Di Tian <sup>4</sup>, Bo Han <sup>1,2</sup>, Shimei Wu <sup>1,2</sup> and Han Zhang <sup>4,\*</sup> 

<sup>1</sup> School of Atmospheric Sciences, and Guangdong Province Key Laboratory for Climate Change and Natural Disaster Studies, Sun Yat-sen University, Zhuhai 519082, China; wurenhao@mail.sysu.edu.cn (R.W.); yangqh25@mail.sysu.edu.cn (Q.Y.); hanbo5@mail.sysu.edu.cn (B.H.); wushm28@mail.sysu.edu.cn (S.W.)

<sup>2</sup> Southern Marine Science and Engineering Guangdong Laboratory (Zhuhai), Zhuhai 519082, China

<sup>3</sup> State Key Laboratory of Numerical Modeling for Atmospheric Sciences and Geophysical Fluid Dynamics, Institute of Atmospheric Physics, Chinese Academy of Sciences, Beijing 100039, China

<sup>4</sup> State Key Laboratory of Satellite Ocean Environment Dynamics, Second Institute of Oceanography, Ministry of Natural Resources, Hangzhou 310012, China; tiandi@sio.org.cn

\* Correspondence: zhanghan@sio.org.cn

Received: 29 September 2019; Accepted: 4 November 2019; Published: 7 November 2019



**Abstract:** The oceanic response of the Taiwan Strait (TWS) to Typhoon Nesat (2017) was investigated using a fully coupled atmosphere-ocean-wave model (COAWST) verified by observations. Ocean currents in the TWS changed drastically in response to significant wind variation during the typhoon. The response of ocean currents was characterised by a flow pattern generally consistent with the Ekman boundary layer theory, with north-eastward volume transport being significantly modified by the storm. Model results also reveal that the western TWS experienced the maximum generated storm surge, whereas the east side experienced only moderate storm surge. Heat budget analysis indicated that surface heat flux, vertical diffusion, and total advection all contributed to changes in water temperature in the upper 30 m with advection primarily affecting lower depths during the storm. Momentum balance analysis shows that along-shore volume acceleration was largely determined by a combined effect of surface wind stress and bottom stress. Cross-shore directional terms of pressure gradient and Coriolis acceleration were dominant throughout the model run, indicating that the effect of the storm on geostrophic balance was small. This work provides a detailed analysis of TWS water response to typhoon passage across the strait, which will aid in regional disaster management.

**Keywords:** Taiwan Strait; Typhoon Nesat; coupled atmosphere-ocean-wave model; volume transport; momentum balance analysis; heat budget

## 1. Introduction

A typhoon, the Western North Pacific version of a hurricane, represents one of the most severe weather events on Earth. When a typhoon makes landfall, the associated strong winds and heavy precipitation can cause devastating loss of life and property. In order to minimise the damage induced by typhoons, accurate predictions for the track and intensity of individual typhoon systems are of great importance. A thorough understanding of air–sea interaction processes during a storm is essential to make a reliable prediction. Within the past two decades, extensive research on the deep ocean response to typhoons has taken place (e.g., [1–7]). In contrast, the impact of a typhoon on coastal waters has been relatively less studied (e.g., [8,9]). Coastal waters yield an important influence on the intensity of a typhoon approaching landfall. At the same time, a typhoon will also strongly enhance vertical mixing in the near-shore waters, influence volume and heat transport in both along- and cross-shore directions, and alter the marine environment in many ways (e.g., [8,9]). Here, we examine the response

of coastal water in the Taiwan Strait (TWS, Figure 1) following the crossing of Typhoon Nesat in 2017. This typhoon is chosen just because there are relatively more field observations for validating our model results.

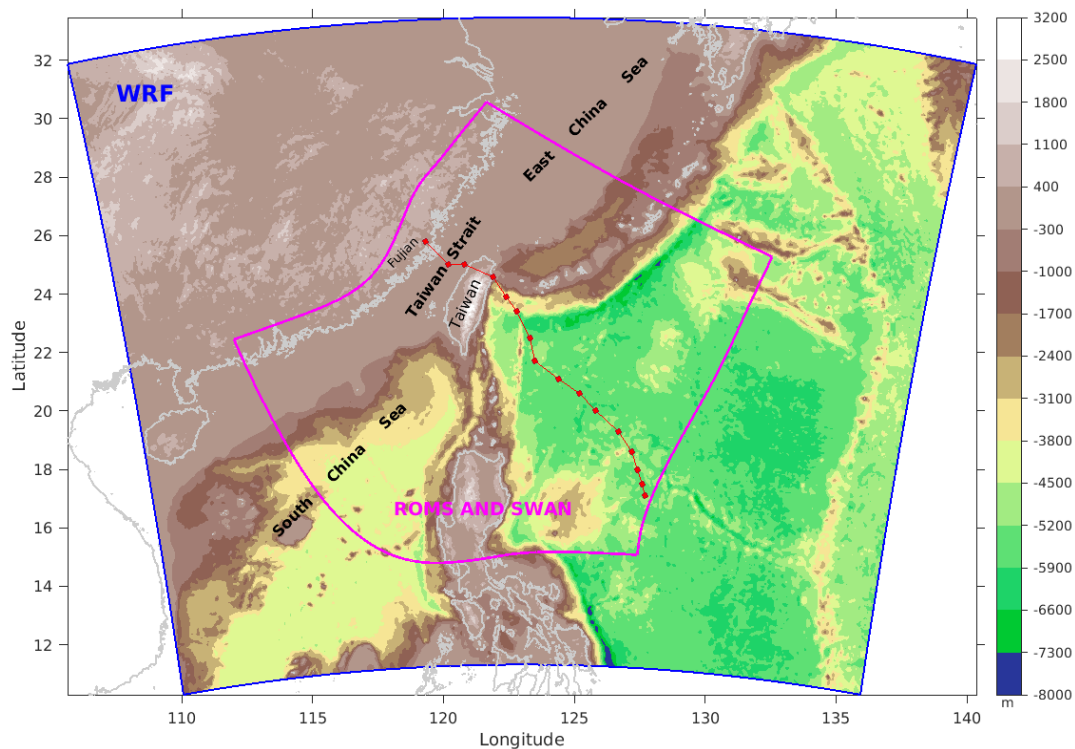


**Figure 1.** Location map showing the track (red squares) at six hour intervals of Typhoon Nesat (2017). Model domain for the Regional Ocean Modelling System (ROMS) and Simulating Waves Nearshore (SWAN) is bounded by pink curves, the domain for Weather Research and Forecasting (WRF) is shown in blue. Colour scale represents the bathymetry of the ocean and land topography height.

TWS is oriented in a south-west–north-east direction (Figure 1), connecting the East China Sea (ECS) in the north-east and South China Sea (SCS) in the south-west, with a width of  $\sim 180$  km, length of  $\sim 350$  km, and an average depth of  $\sim 60$  m. Tides within the strait are propagated from both the ECS and SCS, with an M2 tide being the dominant constituent [10–14]. Volume transport through TWS shows strong seasonal variations which are at a minimum in winter and a maximum in summer [15–17], with the annual mean transport being in a northward direction from the SCS to the ECS. The East Asian monsoon is thought to be the primary influence on seasonal changes in volume transport [17,18]. Other factors such as sea level slope along the strait [19], synoptic events like typhoons [20], and mesoscale eddies [21] can also influence the transport. Subtidal currents flow mainly north-eastward during summer, fed by South China Sea water. In contrast, winter flow consists of a southward current along the west side carrying colder China Coastal water, and a northward current fed by the Kuroshio Branch along the east side [22–24].

The TWS is one of the main passages for typhoons in the coastal waters of China (cf. Figure 2 in [25]), yet despite their impact on the environment of the TWS, studies are still limited. Research within the last decade has focused on analysis of storm surges [26,27], the importance of tide–surge or wave–tide–surge interactions in predicting the storm tide [25], or consideration of volume transport [20], sediment transport [28]), and currents [29,30]. In this study, a fully coupled ocean–atmosphere–wave model system [31] with a high horizontal resolution ( $\sim 1$  km) is employed to investigate the response of the TWS to Typhoon Nesat (2017). The volume transport, heat budget, and momentum balance will be discussed in detail. A fully coupled modelling system should present more complete results than uncoupled modelling systems used in previous studies (e.g., [26]) as it not only utilises ocean and

wave models that are forced by atmospheric conditions with sufficiently high spatial and temporal resolution, but also provides feedback to the atmosphere model.

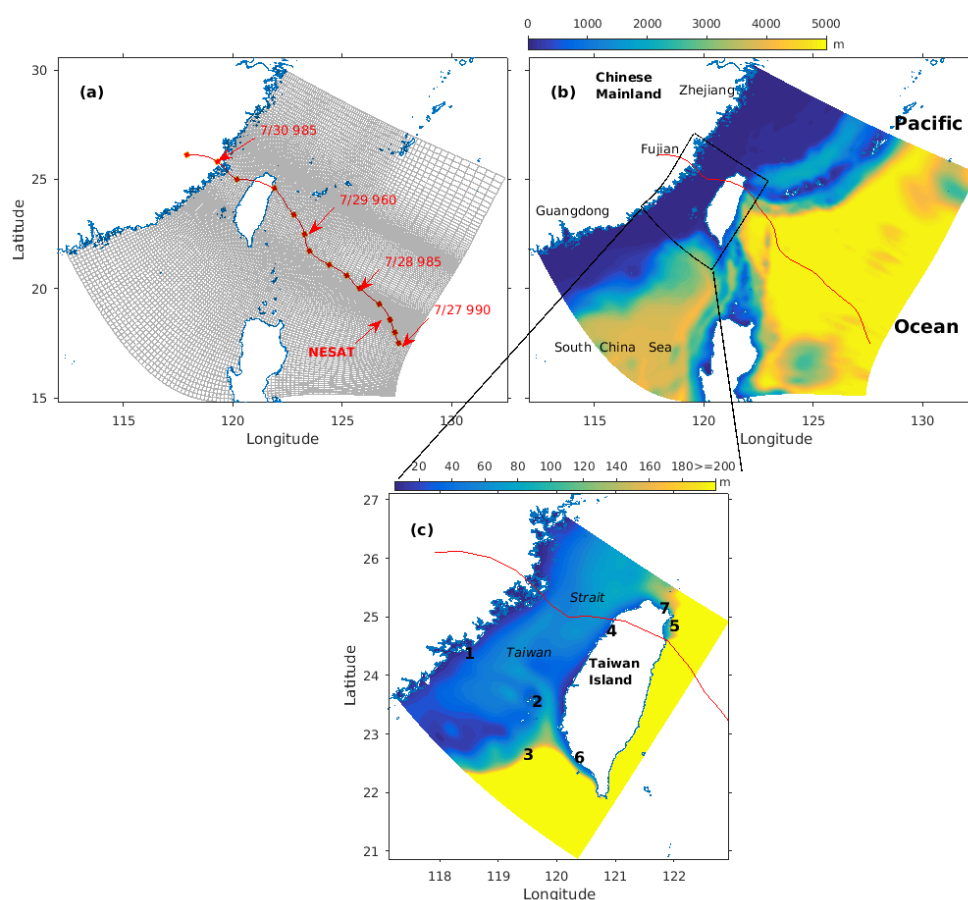


**Figure 2.** The distribution of model grids and bathymetry for ROMS and SWAN. (a) Model grid distribution showing track of Typhoon Nesat over six hour intervals (red squares) on 27–30 July, 2017, (b) regional bathymetry, and (c) enlarged image of bathymetry for the Taiwan Strait with numbers 1–7 denoting sites of in situ observational stations. The red curve in each subplot is the track of Nesat.

## 2. Materials and Methods

### 2.1. Observational Datasets

Time series data for Typhoon Nesat’s centre location and pressure at sea level at 6 h intervals were obtained from the best track data issued by the Japan Meteorological Agency (JMA) (Figure 2a). Microwave-only (MWO) SST daily products [32] were used to adjust the modelled SST. Tide gauge and moored buoy data were obtained from the Central Weather Bureau (CWB), Taiwan (<https://www.cwb.gov.tw/V7/observe/marine/>). The observation stations were numbered as shown in the panel expanded from the regional bathymetry image of Figure 2b, and are denoted by the numbers 1–7 (Figure 2c). These gauges and buoys provided oceanographic and meteorological data such as water and air temperature, air pressure at sea level, wave height, and wind speed. It is worth mentioning that the exact positions of some stations (e.g., stations 6 and 7) were not resolved in ROMS and SWAN models due to their proximity to the shoreline; therefore, the water-covered model grid points nearest to these stations were selected for the comparison between model results and observations. Jason-2 altimeters were used to calculate significant wave height. Only observations from the Ku band were used in this study because they have higher accuracy than observations from the C band (<http://globwave.ifremer.fr/products/>) [33].

## 2.2. Typhoon Nesat

Typhoon Nesat started as a tropical depression east of the Philippines on 25 July, 2017. It gradually intensified as it tracked north-westward. By the morning of 27 July, the JMA upgraded Nesat to a severe tropical storm. Nesat reached Category 1 Typhoon status at around 0600 UTC on 28 July, reaching its peak intensity later that day as a Category 2 Typhoon with a central pressure of 960 mbar and 10 min maximum sustained winds of  $42 \text{ m s}^{-1}$ . On 29 July, Nesat made its first landfall at Taiwan Island. Several hours later, it crossed Taiwan Island and subsequently downgraded to a tropical storm as it continued moving to the west in the TWS. At around 2200 UTC on 29 July, Nesat made its second landfall at coastal Fujian Province, mainland China.

## 2.3. Coupled Model

The coupled ocean-atmosphere-wave-sediment transport (COAWST) modelling system [31,34] was adopted for this study. Previous studies (e.g., [35,36]) demonstrate that a coupled model is essential for the better simulations of tropical storms (especially their intensity). Furthermore, a coupled model may do better in the simulation of SST gradients even on a small scale (e.g., 10~100 km) as pointed by [37–42]. The COAWST coupling system is a synergy of three state-of-the-art modelling components: the Regional Ocean Modelling System (ROMS; <http://www.myroms.org/> [43,44]), the Weather Research and Forecasting (WRF) atmospheric model [45], and the spectral wave model SWAN [46]. The three model components communicate with each other through the Model Coupling Toolkit [34]. Although widely used in many realistic case studies (e.g., [47–49]), application of COAWST in Chinese near-shore waters is limited (e.g., [50–52]).

### 2.3.1. WRF Atmospheric Model

The COAWST modelling system adopts the Advanced Research WRF (ARW) dynamic core, which provides several options for physical parameterisation of subgrid-scale processes for simulating mesoscale and microscale motion. Bottom roughness is closely related to the computation of exchange coefficients for heat and momentum in the surface layer [45], hence playing an important role in simulations of tropical cyclones intensity. In COAWST, bottom roughness is modified in the WRF code to take the impact from surface waves [31] into account. For the present study, the WRF model is run on a horizontal grid with a spacing of 6 km that covers most of the western Pacific Ocean that encompass the track of Typhoon Nesat, with track regions located in the centre of the domain (Figure 1). There are 28 sigma levels in the vertical dimension.

Subgrid-scale convection and cloud detrainment are simulated by The Kain–Fritsch cumulus convection scheme [53]. The WRF single-moment six-class (vapor, cloud, rain, snow, ice, and graupel) moisture microphysics scheme was chosen to parameterize grid-scale precipitation processes. Long-wave and short-wave radiation physics were computed by the Rapid Radiative Transfer Model [54] and the Dudhia scheme [55], respectively. For the boundary layer, estimation of sea surface roughness with wave effects in COAWST was performed by the following two methods (see also [49]): a 2.5-order scheme based on the Mellor–Yamada–Nakanishi–Niino scheme [56,57] that is applicable to a variety of different static stability regimes [58], and a 1.5-order Mellor–Yamada–Janjić scheme [59,60]. For this study, the Mellor–Yamada–Nakanishi–Niino scheme, combined with the Eta similarity surface layer scheme [61] and the unified Noah land surface model [62], was adopted. Coupling between the ocean model (ROMS) and WRF model is accomplished by the following two schemes: (1) Feedback from the ROMS to the WRF model through Sea Surface Temperature (SST) with high temporal and spatial resolutions. If the coupling is not activated, the lower resolution (0.5 degree) daily Real-Time Global (RTG) SST field would be used, which can be downloaded from <ftp://polar.ncep.noaa.gov/pub/history/sst> [63]. It should be noted that, here, for simplicity and focusing the key scientific problems (e.g., we only focus on the impact of Nesat in the TWS), we just followed the methods proposed by some previous studies (e.g., [31]) to prescribe SST in the coupled model, as

experiments on model results sensitive to different model settings (e.g., [49]) including using different ways to prescribe SST in the coupled models are of scientific and practical significance, which will be discussed especially in another manuscript. (2) Forcing of ROMS using momentum and heat flux by the WRF model. A flux-conservative remapping scheme in COAWST was implemented, so that both ROMS and the WRF model used the same fluxes at the atmosphere–ocean interface.

The interaction between the SWAN model and the WRF model occurs as follows: (1) the WRF model drives the SWAN model by supplying wind forcing and (2) the peak periods, peak wavelengths, and significant wave heights are fed to the WRF model by SWAN for calculation of the wave-induced surface roughness at the sea surface. We used the scheme proposed by Taylor and Yelland [64] to estimate the wave-enhanced bottom roughness in this study.

The WRF model is initialised and forced by data from National Centers for Environmental Prediction (NCEP) Final Operational Global Analysis data (FNL) (<http://rda.ucar.edu/datasets/ds083.2/>) [65], with a 1° horizontal resolution and 6 h time intervals. To further improve the simulation for the typhoon track and intensity in this study, a spectral nudging scheme [66] was applied to the horizontal wind, temperature, and geopotential height in the upper layer ( $k > 10$ ) of the GFS data. A nudging coefficient of  $0.0003 \text{ s}^{-1}$ , indicating a relaxation time of approximately 1 h, was used for all nudging variables. A wave number of 3 was used for both the zonal and meridional directions, resulting in waves with wavelengths equal to or greater than approximately 900 km being nudged. Nudging was performed every 6 h during the entire simulation. The total run time for all three model components was 12 days (i.e., from 0000 UTC on 24 July to 0000 UTC on 5 August). We did not use any scheme (e.g., [31]) to re-strengthen the initial intensity in the simulation because the GFS data would not have been able to be used to adequately simulate typhoons. The intensity of the modelled Typhoon Nesat was very close to observations after a spin up of 1 day (Figure 3).

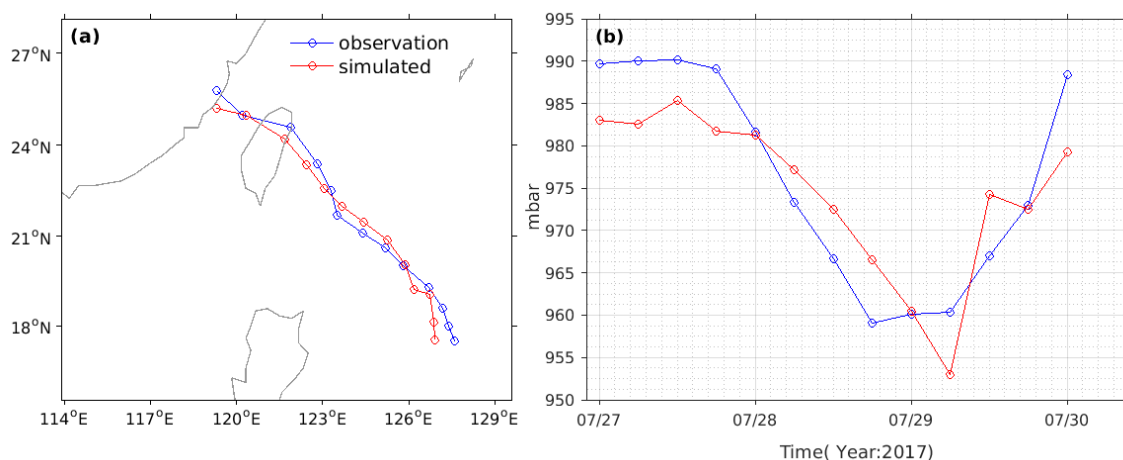


**Figure 3.** Comparison between simulated and observed typhoon (a) tracks and (b) intensities. Here, the Japan Meteorological Agency (JMA) best track data was used, with the coloured blue circles in (a) denoting the typhoon centre position every six hours starting at 0000 UTC on 27 July 2017.

### 2.3.2. ROMS Ocean Model

ROMS is a free-surface, terrain-following, three-dimensional ocean model. The details of the numerical algorithm for ROMS can be found in [44]. The code for ROMS is written with high flexibility, offering a wide range of solution algorithms for pressure gradient and horizontal and vertical advections, as well as subgrid-scale parameterisations.

The ROMS model domain is shown in Figure 1, covering the coastal waters of Southeast China, parts of northern South China Sea, and north-western Pacific Ocean. Horizontally, the domain is discretised by orthogonal curvilinear grids with a  $376 \times 538$  array for the horizontal coordinates ( $x, y$ ). Horizontal resolution in the Taiwan Strait is highest with a minimum grid spacing of  $\sim 970$  m.

For other regions, the grid spacing is in the range of 1–12 km. Vertically, 40 levels are used for the stretched terrain-following coordinate. The vertical stretching parameters  $\theta_s = 6.5$ ,  $\theta_b = 2.5$  and  $T_{\text{cline}} = 100$  m were selected to better resolve the surface and bottom boundary layer structures. The water depths in the model domain were derived from the General Bathymetric Chart of the Oceans (GEBCO) bathymetry data with 30 s spatial resolution [67] by smoothing to ensure the maximum slope  $r - \nabla h/h$  to be less than 0.35 [68,69].

The model was initialised with the output of HYbrid Coordinate Ocean Model (HYCOM) GLBu0.08 [70]. The open boundary conditions for currents, temperature, and salinity are also taken from the output of HYCOM. Thirteen tidal constituents—K1, O1, P1, Q1, K2, M2, N2, S2, MF, MM, M4, MS4, and MN4 [71] were applied as the tidal forcing. The open boundary conditions were as follows: Chapman conditions for the free surface, Flather conditions for the two-dimensional momentum, radiation plus nudging conditions for the three-dimensional momentum, and temperature and salinity with a 1 day nudging coefficient. The sea surface forcing including momentum and heat fluxes were provided by the WRF model, whereas the ROMS model provided feedback to the WRF model with updated SST. In order to better simulate typhoon intensity, the modelled SSTs were also restored to the microwave observed SST (MVSST, <http://www.remss.com>) [32] by activating the ROMS CPP option of QCORRECTION.

The following effects of surface waves in ROMS were considered: (1) injection of turbulent kinetic energy by wave breaking, which was incorporated into ROMS by the generic length scale method [72] and (2) wave forces. The vortex force approach was used [73]. Although these effects were included in the simulation, we will not discuss them here to avoid distraction and for brevity. The Generic Length Scale (GLS\_MIXING)  $k - \omega$  model mixing scheme [72] was adopted to compute the vertical viscosity and diffusion terms.

We ran the ROMS model twice. In order to examine whether the model was capable of reproducing tides in our study domain, the ROMS model was first run separately forced only by tides with temperature and salinity fixed (barotropic mode) over a total runtime of 35 days. The final 30 day model output was used to compare the simulated co-tide chart with the observed one. Finally, the coupled model of ROMS, WRF, and SWAN was run as described above.

### 2.3.3. SWAN Wave Model

In order to estimate the wave-induced surface roughness at the air–sea interface in the WRF model and the influence of surface waves on ROMS, some wave parameters (e.g., wave length, wave height, wave period, wave direction, and wave breaking) must be provided by the SWAN wave model [46]. The SWAN model effectively solves the wave action balance equation, accounting for wind-wave generation, nonlinear wave-wave interactions, bottom dissipation, wave breaking, shoaling, and refraction.

For the present study, the spatial grid for SWAN was the same as for ROMS (Figure 2), with the wind forcing supplied by the WRF model. Directional space was discretised with 36 directional bins and 24 frequency bins between 0.04 and 1.0 Hz. The boundary conditions were taken from solutions of the WaveWatch III model [74]. SWAN runs in nonstationary mode allowing for changing currents [75] and free surface elevation, dissipation processes (whitecapping, bottom friction), and quadruplet nonlinear wave–wave interactions. Currents and free surface elevation were provided by ROMS. Whitecapping was computed on the basis of Komen et al. [76]. In this fully coupled model simulation, the baroclinic time step was set to 60 s, with a time splitting ratio of 30 for ROMS. SWAN ran with a time step of 300 s, and the WRF model ran with a time step of 30 s. The time interval for data interchange among the models was set to 600 s.

### 3. Results

#### 3.1. Validation for Model Results

##### 3.1.1. Meteorological Parameters

Figure 3 shows the comparisons between simulated and observed tracks and intensities of Typhoon Nesat. The modelled track is generally consistent with the observed track with an average deviation of ~30 km from observations, which is fairly accurate in view of some previous studies (e.g., ~100 km in [77]). It is thought that large-scale synoptic atmospheric circulation determines the tropical storm track (e.g., [78]). The spectral nudging scheme applied in this study ensures that the large-scale atmospheric circulation simulated by the WRF model remains similar to observations or analysis, therefore significantly improving the simulation of the track of the typhoon [79]. With regard to the translation speed of the storm, the deviation of model results from observations is overall small, except on 27 July, when the deviation is larger (see the coloured circles in Figure 3a). The differences between the time series of simulated sea level pressure at the storm centre and those from the JMA data were also small between 27 and 30 July with a mean deviation of ~4.6 mbar (Figure 3b).

In order to further validate the WRF model performance, we computed the root mean square error (RMSE) and correlation coefficients (CC) between the simulated and observed sea level pressure and wind speed (Figure 4) at five stations (Figure 2c). For sea level pressure, model predicted values are overall very close to their observed counterparts with similar trends at all five stations, which are particularly true before or after the storm. However, during the storm (28 July–31 July), small deviations between modelled and observed sea level pressure were found at all stations mainly due to small errors in the simulated storm track. For wind speed, there are some notable features worth mentioning: (1) The simulated wind speeds agreed well with the observations at Stations 3–5 (relatively high CC), while only moderately at Stations 1 and 2 (relatively low CC); (2) the centre of the storm passed over Station 4, which can be confirmed by the double peaks in wind speed in both model results and observations. Additionally, the modelled maximum wind speed is larger than that from observations at Station 4 owing to the simulated storm track being much closer to Station 4; (3) for Station 5, which is located to the north of Nesat's track, time evolution for both the simulated and observed wind speeds showed more regularity than those on the south side (Stations 1, 2, and 3). Overall, the storm was well reproduced in the WRF model, particularly in terms of its track and intensity, hence allowing us to confidently investigate the ocean responses in the following sections.

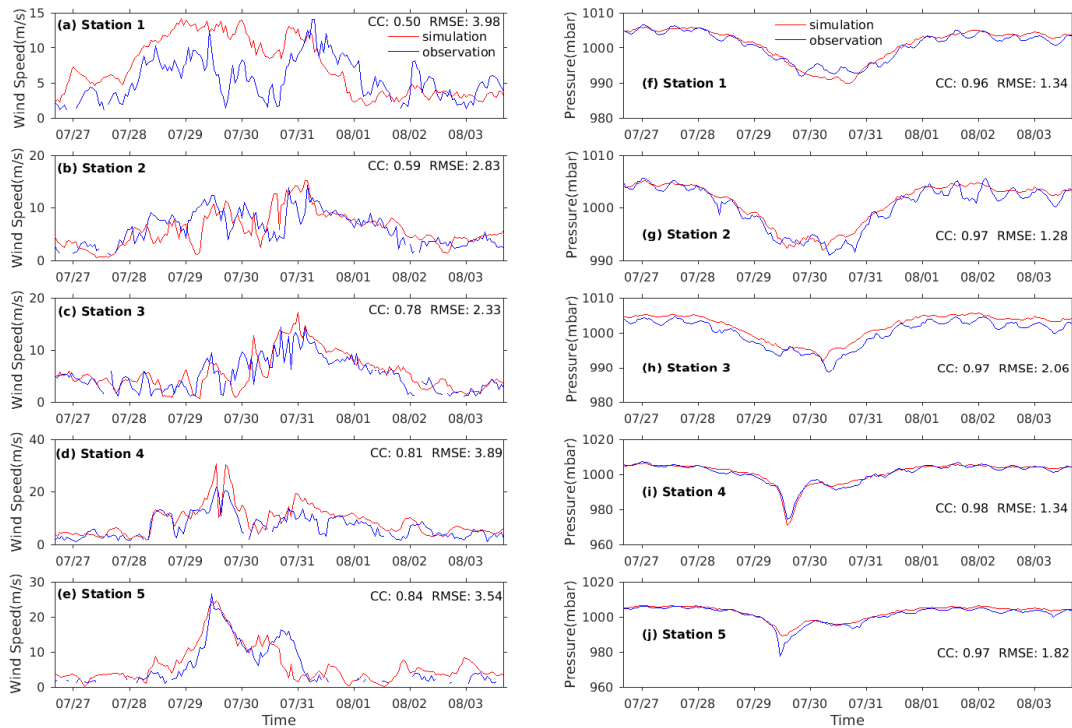


**Figure 4.** Comparison of time series of WRF simulated (red lines) and buoys observed (blue lines) of wind speed (a–e) and air pressure at sea level (f–j). CC denotes the correlation coefficient, RMSE is the root mean square error. The positions of stations are shown in Figure 2c.

### 3.1.2. Tides

Tidal waves and currents are the main aspects of hydrodynamics of the TWS, with the semi-diurnal M2 tide being the dominant constituent. For studies on storm surges in this region, accurate simulations of tidal motions are essential. The co-tidal chart of the M2 tide is shown in Figure 5. Overall, patterns of co-phase lines and contours of co-amplitude are consistent with previous studies (e.g., [13,80]) and the co-tidal charts in the Marine Atlas of the Bohai Sea, Yellow Sea, and East China Sea [81]. It can be seen that the M2 tidal amplitude has a range of 0.4–2.5 m in the TWS, with an enhanced amplitude occurring along the west flank due to an expected Coriolis effect. The M2 tidal wave is characterised by a south-westward-propagating Kelvin wave along the west coast and a standing wave in the south-west region of the TWS.

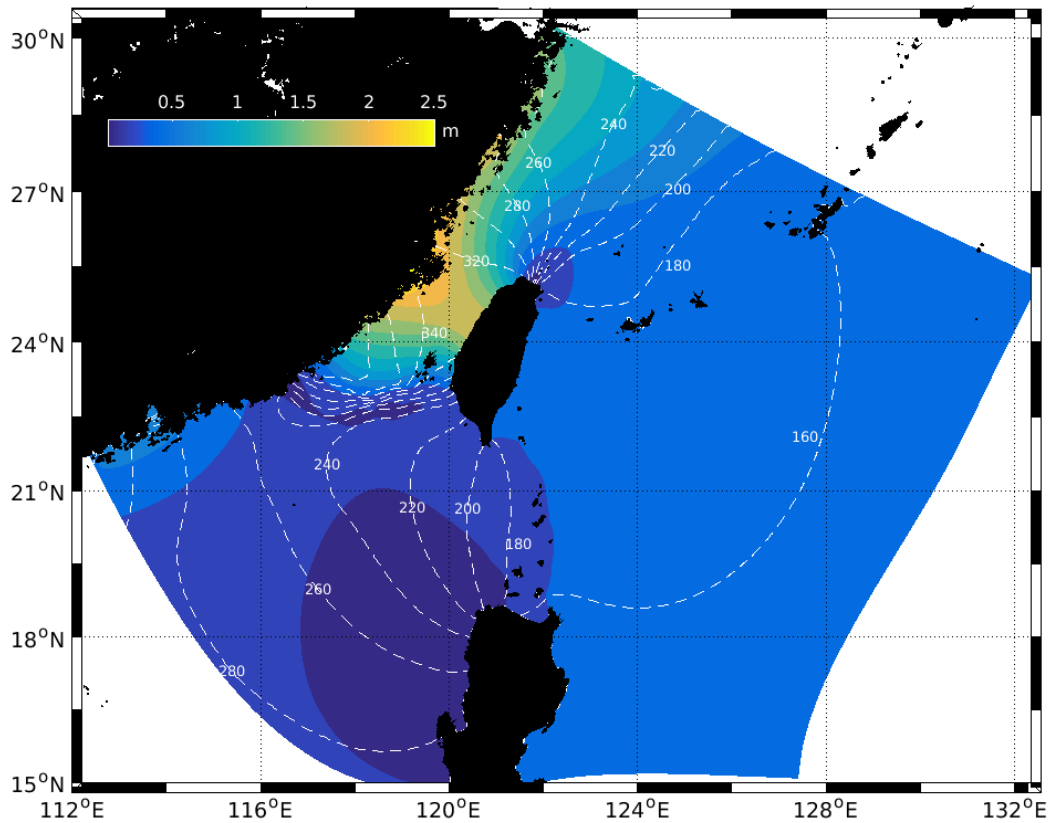


**Figure 5.** The co-tide chart for the M2 tide based on the output of the ROMS model forced only by tides. Dashed lines denote phase while shading colours represent amplitude.

In order to further assess the performance of ROMS in simulating tides in this region, we compare the model-based harmonic constants for the M2 and K1 tidal constituents with those from three stations (Table 1). In this instance the model results are from the fully coupled model run. The errors for M2 tidal amplitude are 0.4, 11, and 5.64 cm, and the errors for the M2 tidal phase are 4.87°, 8.95°, and 6.05°, for Stations 2, 6, and 7, respectively. The relatively large difference in amplitude at Station 7 may be due to the complex coastline and bathymetry adjacent to this station which is not well resolved in our model. For the K2 tide, the amplitude errors are 3.57, 0.86, and 1.09 cm, and phase errors are 17.11°, 12.63°, and 26.26°, for Stations 2, 7, and 6, respectively. Therefore, the ROMS model has satisfactorily reproduced the main tidal features in this region hence allowing us to do further analysis.

**Table 1.** Model-data validation of amplitudes and phases of the M2 and K1 tidal constituents at three gauge stations. The ROMS model results are based on the fully coupled case.

		M <sub>2</sub>		K <sub>1</sub>	
		Amplitude(cm)	Phase (°)	Amplitude(cm)	Phase (°)
Station 2	Observation	87.17	328.99	18.32	288.12
	Model	86.77	333.86	21.89	271.01
Station 7	Observation	20.31	264.90	14.69	210.81
	Model	9.31	273.85	15.55	198.18
Station 6	Observation	12.64	57.63	12.26	223.17
	Model	18.28	51.58	11.17	196.91

### 3.1.3. Surface Waves

Figure 6 displays the comparison between significant wave height ( $H_s$ ) from the SWAN model as observed at Stations 2, 3, and 5. Stations 2 and 3 are located on the south side of the storm track,

far from the Radius of Maximum Wind (RMW), while Station 5 is situated on the north side close to the RMW. It can be seen that, overall, the simulated results are consistent with the observations, with a RMSE for  $H_s$  of about 0.51, 0.55, and 0.92 m, and corresponding correlation coefficients of 0.74, 0.94, and 0.90, for Stations 2, 3, and 5, respectively, for the entire simulation. However, notable deviations between the simulated and observed results were found during the storm at all three stations, especially at Station 2, which are attributed to errors in the modelled storm translation speed, track, and intensity. In addition, because Stations 2 and 5 are in the near-shore region, the coastlines and bathymetry there may not be well-resolved, causing errors in coastal reflected waves.

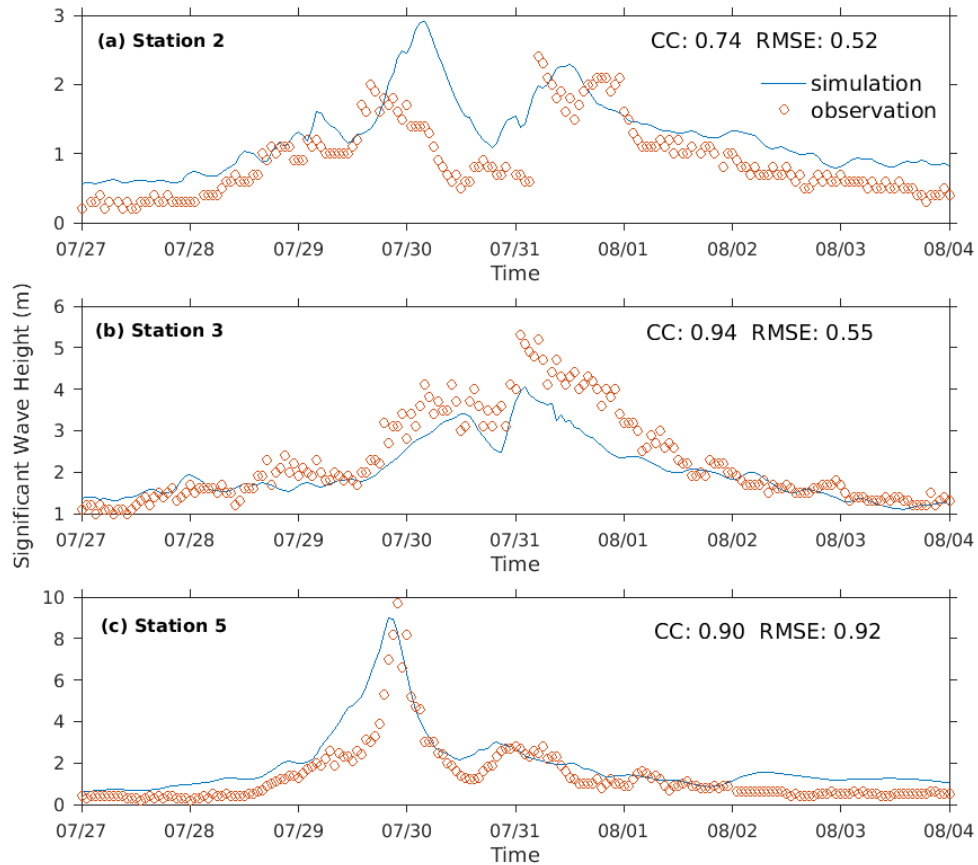


**Figure 6.** Comparison of significant wave height between model and observed data for (a) Station 2, (b) Station 3, and (c) Station 5. CC denotes correlation coefficient, RMSE is the root mean square error. The positions of stations are shown in Figure 2c.

To further validate the wave model results, the simulated significant wave height,  $H_s$ , was compared with that from the Jason-2 Ku band data (Figure 7). The agreement is overall good, with a slope of the regression line of approximately 1.13 with a bias of approximately  $-0.46$  m, indicating that the  $H_s$  values are underestimated by the model. Note that the modelled and measured results show increasing dispersion with  $H_s$ . This might be induced by the frequency of model output, model grid resolution, and the method used to estimate  $H_s$  from satellite data [82].

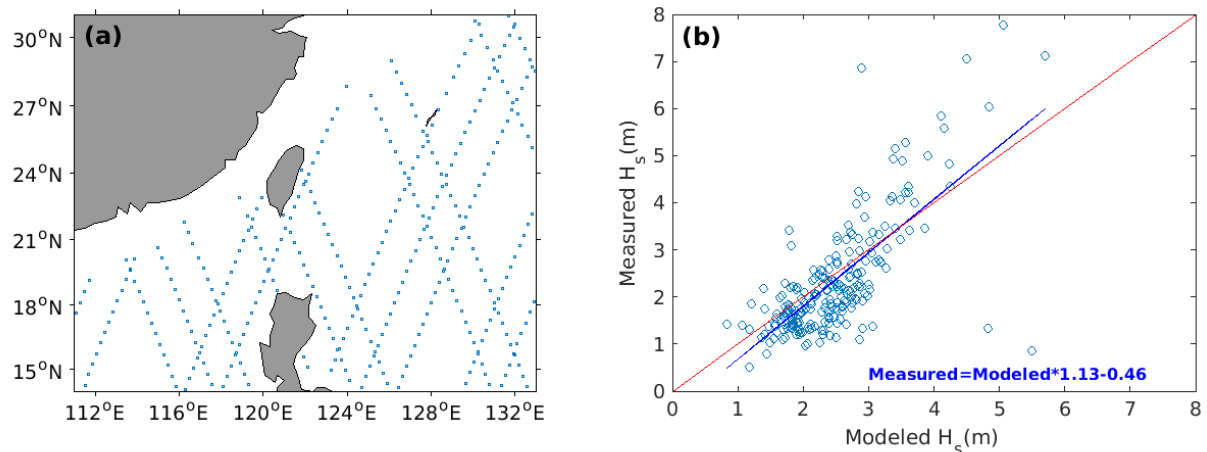


**Figure 7.** Comparison between Jason-2 observed  $H_s$  and simulated  $H_s$ : (a) ground track of the Jason-2 satellite from 0000 UTC on 26 July to 0000 UTC on 5 August and the study region; (b) significant wave height scatter plot, comparing model results and Jason-2 altimeter data.

## 4. Discussion

### 4.1. The Surface Current and Volume Transport Responses

In order to highlight the impact of Typhoon Nesat on the TWS, we plotted the wind and ocean surface current fields for three representative time periods: 24 July, before the storm; 29 July, during the storm; and 31 July, after landfall. We drew the ocean surface wind and current fields for 24 July based on the Cross-Calibrated Multi-Platform (CCMP) wind data and HYCOM model output, respectively, as our coupled model needed to have an initial adjustment on this day. The distribution of the CCMP daily wind on 24 July (Figure 8a) clearly shows a typical summer south-west monsoon pattern such that, prior to the approach of Typhoon Nesat, mild winds of about  $2 \text{ m s}^{-1}$  prevailed over the TWS, with the ocean surface current generally flowing north-eastward at a speed mostly less than  $0.5 \text{ m s}^{-1}$  (Figure 8d). When the centre of storm, with a well-organised cyclonic wind structure, made its approach to the TWS on 29 July, wind speed increased to  $10\text{--}15 \text{ m s}^{-1}$  (Figure 8b). Under the influence of such a storm wind pattern, the currents in the TWS were dramatically modified to a flow pattern largely following the classic Ekman theory, e.g., flow at a  $45^\circ$  angle to the right of the wind in the Northern Hemisphere. Furthermore, a cyclonic eddy-like flow structure was also observed in the middle of the TWS. On 31 July, Nesat made landfall for the second time along the coast of Fujian Province, accompanied by a strong south-westerly wind in the TWS that was significantly larger than the pre-storm maximum wind speed ( $\sim 4 \text{ m s}^{-1}$ ), with a maximum speed of up to  $18 \text{ m s}^{-1}$  (Figure 8c). The ocean surface current conditions were restored to a pre-storm pattern on 31 July but with notably enhanced speed (Figure 8f), likely induced by the intensified south-westerly wind compared to pre-storm conditions. This suggests that the wind and current field over the TWS changed dramatically and rapidly during the passage of a storm. Based on drifter observations, Chang et al. [29] reported a similar current response to the passage of Typhoon Hai-Tang (2005), which had a track similar to Nesat (2017). However, here we provide a more detailed spatial structure of the surface current response.

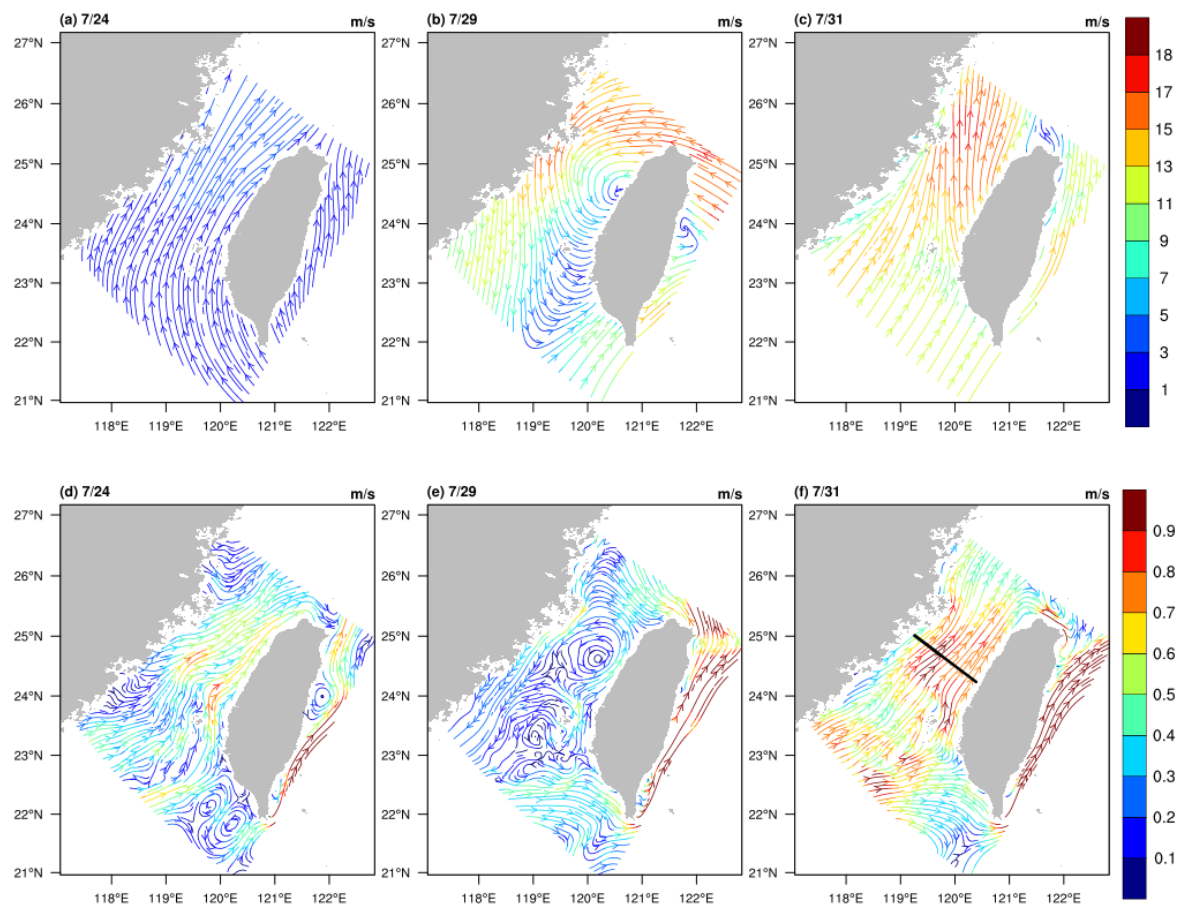


**Figure 8.** Top panels: daily averaged wind field from CCMP wind data from WRF simulation for the dates of (a) 24 July, (b) 29 July, and (c) 31 July. Bottom panels: daily averaged ocean surface currents from ROMS simulation for the dates of (d) 24 July, (e) 29 July, and (f) 31 July. Colours represent the velocity magnitude. The straight black line in (f) denotes the position of a cross-section analysed in Figures 9–13.

We next consider the dynamic response to the passage of Nesat in the water column. For this purpose, changes of the along-shore current velocity averaged over a selected cross-section, indicated by the straight black line in Figure 8f, with time (Figure 9a) are examined. Before the storm (before 28 July), the flow structure in the TWS was dominated by barotropic tidal currents, whereas the storm itself (28 July–1 August) affected the entire water column, including barotropic and baroclinic flow structures. It is evident that the south-westward current (negative) was enhanced when the storm approached the TWS, in contrast to the intensification of the north-eastward current (positive) during the departure of storm. By 2 August, the entire water column current structure was restored to its pre-storm pattern (tidally dominated).

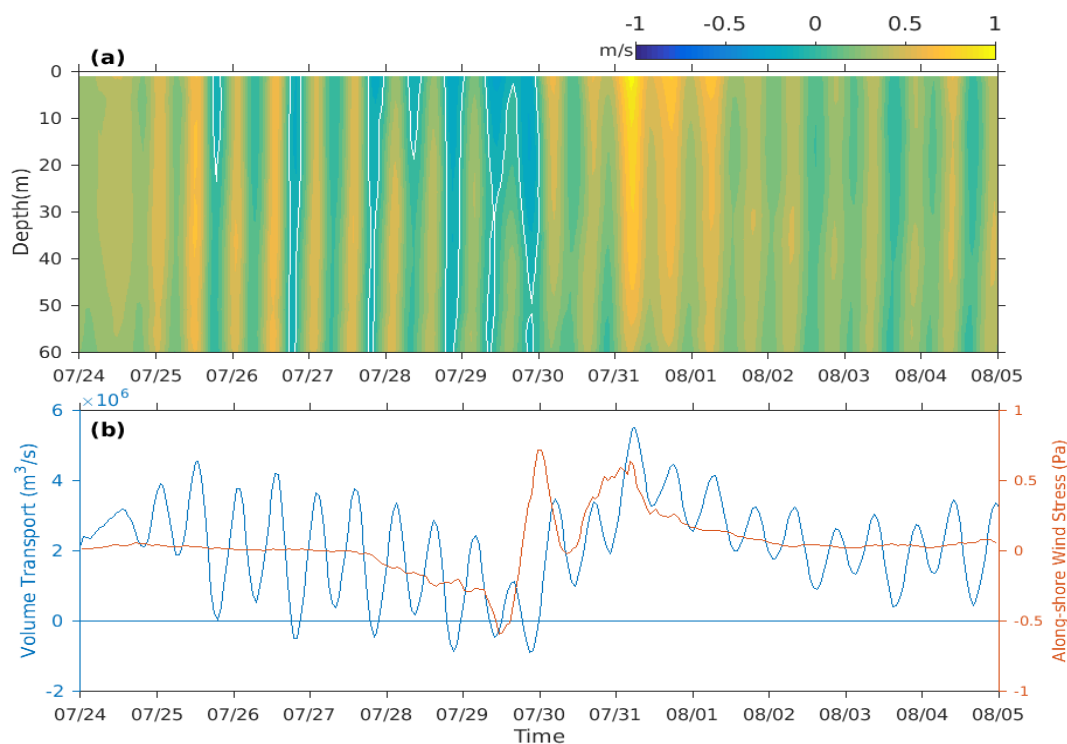


**Figure 9.** Averaged current velocity over time before, during, and after the passage of Typhoon Nesat, from the cross-section indicated in Figure 8f: (a) averaged along-shore velocity changes with time and depth, (b) time series of volume transport through the same cross-section (blue line) and cross-section averaged surface along-shore wind stress (red line).

Volume transport through the TWS plays a crucial role in the water exchange between the SCS and the ECS. The monthly mean transport is mainly north-eastward (toward the ECS) in summer and is notably reduced or even reversed in winter [15,17,23]. Undoubtedly, a storm crossing the TWS will strongly influence the volume transport. The time series of volume transport through the selected cross-section is shown in Figure 9b, overlain by the averaged along-shore surface wind stress. The estimated volume transport is not sensitive to the location of a cross-section in the TWS. It can be seen that the variations of volume transport are dominated by tidal motions before the storm with a mean tide-free positive value around  $2.1 \times 10^6 \text{ m}^3 \text{ s}^{-1}$ , indicating a typical summertime volume transport value through the TWS consistent with previous observational studies [17,83]. When the storm approached, the north-eastward volume transport was significantly reduced, or even temporally reversed, in response to the along-shore wind stress (Figure 9b, red line). When the storm made landfall for the second time on the coast of Fujian Province (after 30 July), the intensified winds were from the south-west, resulting in the rapid restoration of north-eastward volume transport to its pre-storm level. It should be noted that after 30 July the winds experienced a second peak which was induced by the passage of another storm, Hai-Tang [84], after Nesat. Interestingly, under the influence of the second south-west wind maximum (roughly on 31 July), the north-eastward volume transport was temporally increased by as much as 50% compared to the mean level. After the second positive peak, the wind gradually returned to its pre-storm condition followed by a restoration of the ocean volume transport.

From the above analysis, we can see that local wind variations play a major role in modifying volume transport. The correlation between along-shore wind stress and volume transport is 0.8 with a confidence level of 99%, which confirms the leading role played by the local wind. In an investigation into the enhancement of northward transport through the TWS by typhoons, Zhang et al. [20] pointed out that the significant change of the ageostrophic effect associated with local atmospheric forces rather than remote forcing during typhoons is the main cause for changes in volume transport.

#### 4.2. Storm Surge

The storm surge is obtained by subtracting predicted tidal oscillations of water level from the simulated storm tide given by the fully coupled model system. Spatial distribution of the maximum storm surge obtained this way is depicted in Figure 10. Model results show that the coastal regions of Fujian Province experienced the largest storm surge generated by Nesat, while the east side of TWS had only moderate storm surge. Additionally, the large surge heights were mainly found in coastal regions directly in right front of Nesat’s landing point. The maximum surge height in the strait occurred in some semi-enclosed bays, reaching up to 2.7 m.

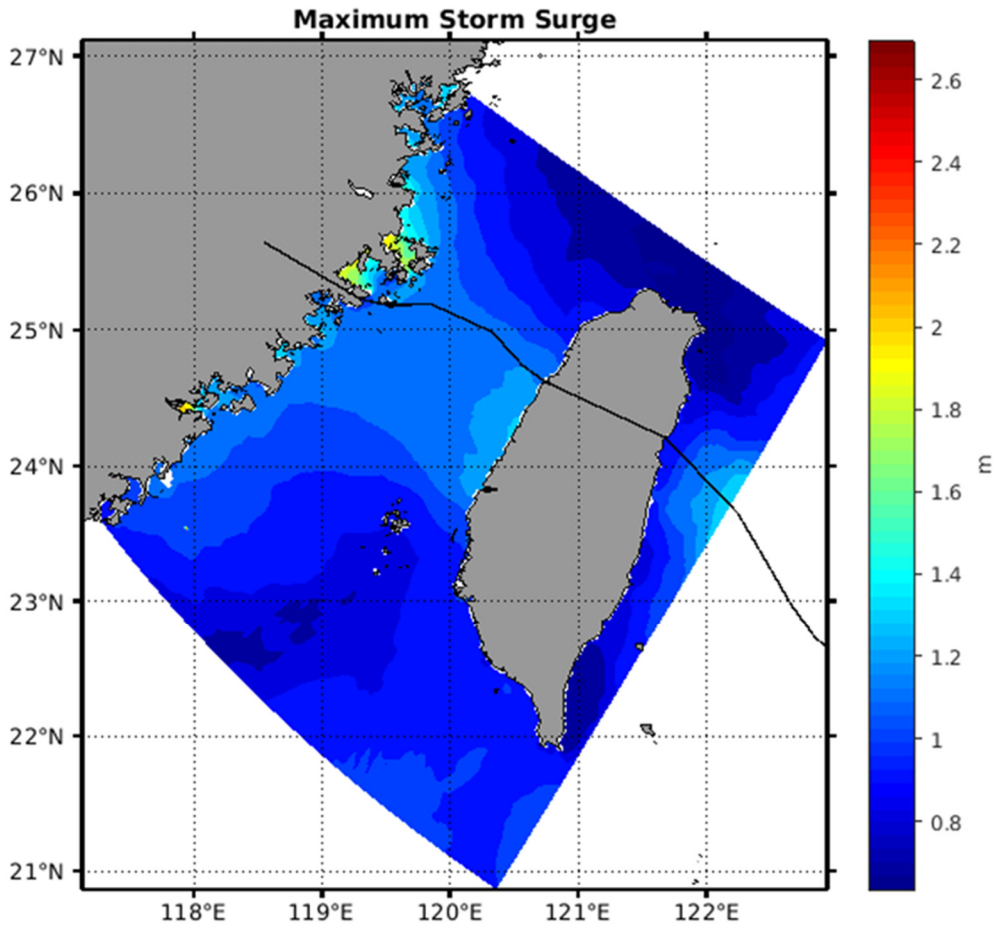


**Figure 10.** Spatial distribution of modelled maximum storm surge. Black line indicates track of Typhoon Nesat.

#### 4.3. Diagnostic Analysis for Heat Budget

The temperature equation derived below was used to analyse the relative contributions of surface heat fluxes, advection, and mixing to the changes in temperature throughout the water column. Each term of the following equation was from the ROMS output:

$$\frac{\partial T}{\partial t} = -\frac{\partial(uT)}{\partial x} - \frac{\partial(vT)}{\partial y} - \frac{\partial(wT)}{\partial z} + \frac{\partial(A_{kt} \frac{\partial T}{\partial z})}{\partial z} + D_T + F_T \tag{1}$$

with the surface and bottom boundary conditions:

$$\left(A_{kt} \frac{\partial T}{\partial z}\right)_{z=0} = \frac{Q_{net}}{\rho_0 C_p} \tag{2}$$

$$\left( A_{kt} \frac{\partial T}{\partial z} \right)_{z=-h} = 0 \tag{3}$$

where  $t$  is time;  $u$  and  $v$  represent velocity in the  $x$  (along-shore) and  $y$  (cross-shore) directions;  $T$  is water temperature;  $w$  is the vertical velocity (in  $z$  direction);  $\rho_0$  is a reference density of  $1025 \text{ kg m}^{-3}$ ; and  $D_T$  and  $F_T$  are the horizontal diffusion and friction terms, respectively, which were neglected in the analysis due to their low values. Additionally,  $A_{kt}$  is the vertical eddy diffusivity,  $Q_{net}$  is the surface heat flux, and  $C_p$  is the specific heat capacity of seawater ( $3895 \text{ J (kg C)}^{-1}$ ).

In Equation (1), the left-hand side is the local rate of change. On the right-hand side, the first two terms are horizontal advectations, the third term is vertical advection, and the fourth term is vertical diffusion. The hourly output from ROMS for these terms contained strong tidal signals. We applied a low-pass filter to remove oscillation signals with periods less than 25 h, in order to focus on the subtidal impact of Nesat. Net surface heat flux, detided time series of water temperature, and its budget terms, averaged over the selected cross-section, are shown in Figure 11.

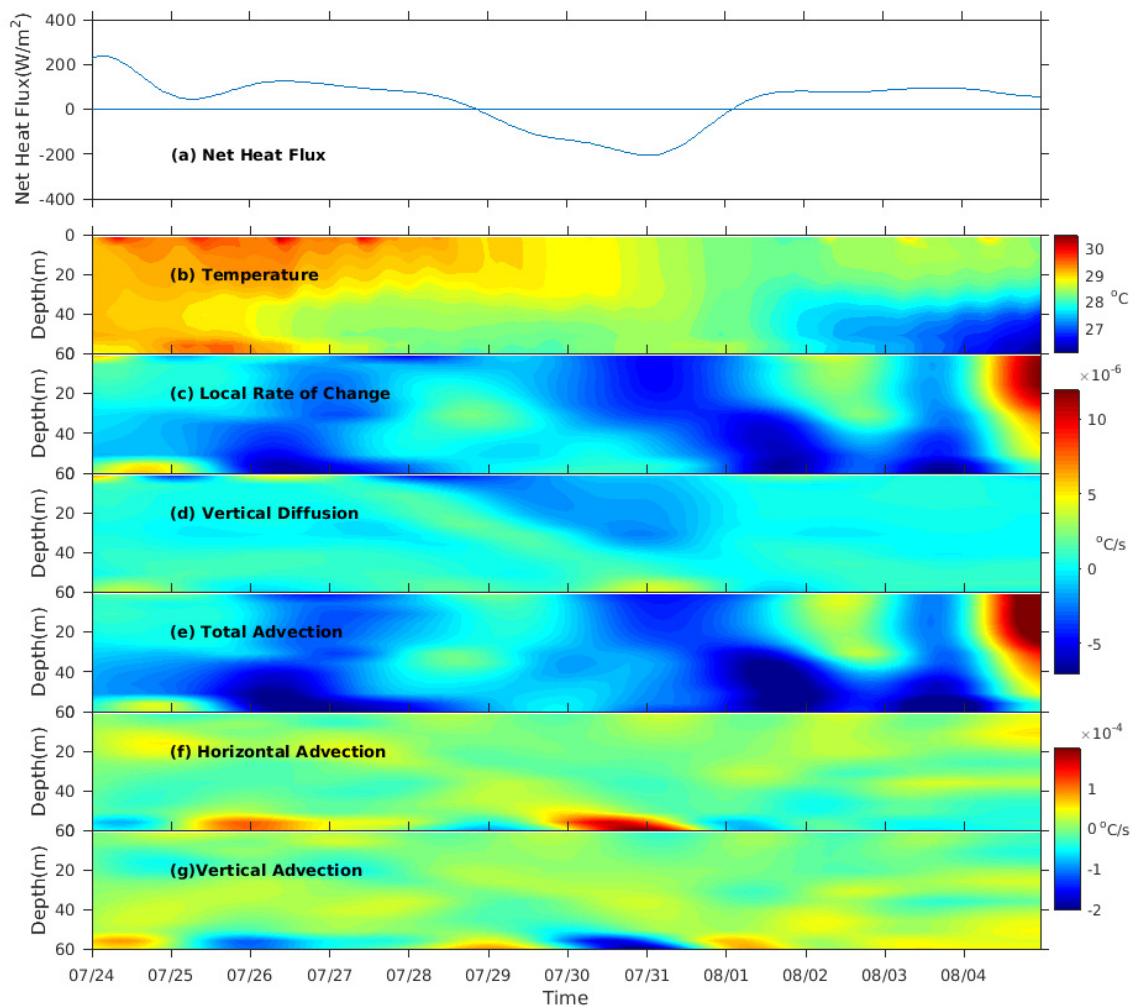


**Figure 11.** Analysis of the TWS cross-section (Figure 8f) averaged water temperature and heat-budget term evolution with time or time and depth: (a) net surface heat flux, (b) water temperature, (c) local rate of change, (d) vertical diffusion, (e) total advection (horizontal + vertical), (f) horizontal advection, and (g) vertical advection. Horizontal and vertical terms are an order of magnitude greater than other budget terms (local rate of change, vertical diffusion, total advection), hence a different colour scale is used.

Before the storm (before 25 July), the net surface heat flux was positive, indicating that the ocean was receiving heat from the atmosphere (Figure 11a). In this scenario the entire water column maintained a nearly uniform temperature of  $\sim 29^\circ\text{C}$ , and the local rate of change of temperature was dominated by advection (Figure 11e). As the storm approached (26–28 July), the surface heat flux gradually declined to zero, allowing advection to cool the water below 30 m depth (Figure 11b). During the direct forcing period (29–30 July), surface heat flux reversed to a negative state, indicative of heat loss that reduced its overall magnitude. During the departure period (30 July–1 August), surface heat loss was further increased, reaching a maximum value on 31 July ( $\sim 200\text{ W m}^{-2}$ ), then gradually reduced to zero (Figure 11a). Vertical mixing led to further cooling of the water column above 40 m depth while warming the layer below. The local rate of change below 40 m depth was dominated by advection, but influenced by a combination of surface heat loss, vertical mixing, and advection in the top 30 m. After the storm (after 1 August), surface heat flux restored to positive values, and the local rate of change of water temperature through the column was once more dominated by the advection. In short, surface heat flux, vertical mixing, and advection all played a part in changing the water temperature in the top 30 m layer, while only advection determined the change of water temperature below this level during the storm.

#### 4.4. Diagnostic Analysis for Momentum Budget

To further examine the processes responsible for the ocean response in TWS to Nesat, a subtidal time series of depth-averaged momentum balance (Figures 12 and 13) was analysed in both along- and across-shore directions. The momentum equations are as follows:

$$\underbrace{\frac{\partial u}{\partial t}}_1 = -\underbrace{\frac{\partial(uu)}{\partial x} - \frac{\partial(vu)}{\partial y}}_2 - \underbrace{\frac{1}{\rho_0} \frac{\partial P}{\partial x}}_3 + \left( \underbrace{\frac{\tau_s^x}{h\rho_0}}_4 - \underbrace{\frac{\tau_b^x}{h\rho_0}}_5 \right) + \underbrace{fv}_6 \quad (4)$$

$$\underbrace{\frac{\partial v}{\partial t}}_1 = -\underbrace{\frac{\partial(uv)}{\partial x} - \frac{\partial(vv)}{\partial y}}_2 - \underbrace{\frac{1}{\rho_0} \frac{\partial P}{\partial y}}_3 + \left( \underbrace{\frac{\tau_s^y}{h\rho_0}}_4 - \underbrace{\frac{\tau_b^y}{h\rho_0}}_5 \right) - \underbrace{fu}_6 \quad (5)$$

where  $u$  and  $v$  are the along-shore and cross-shore components of depth-averaged velocity, respectively.  $P$  is the depth-averaged pressure.  $\tau_s$  and  $\tau_b$  are the surface wind stress and bottom stress,  $h$  is water depth, and  $f$  is Coriolis parameter. Labelled terms include 1—acceleration, 2—horizontal advection, 3—pressure gradient, 4—wind stress, 5—bottom stress and 6—Coriolis force. Horizontal diffusion was small and not considered here.

Wind stress increased prior to landfall and decreased afterwards, with prevailing winds alongshore and slightly offshore toward the south-west prior to landfall. Wind rotation was to the north-east and slightly onshore after landfall. In the along-shore direction, the pressure gradient was balanced by a negative Coriolis term. As the storm was approaching, the south-westward wind stress decelerated the pre-existing north-eastward current, whereas the north-eastward wind stress accelerated the current after landfall. As the storm was leaving, wind stress decreased along with the north-eastward ocean current, as a result of bottom stress. In the cross-shore direction, acceleration was lower than that in the along-shore direction, with the dominant terms of pressure gradient and Coriolis terms throughout the entire model run times indicating that the effect of storm forcing on the geostrophic balance was small. Depth-averaged horizontal advection terms in both along- and cross-shore directions were small (not shown here).

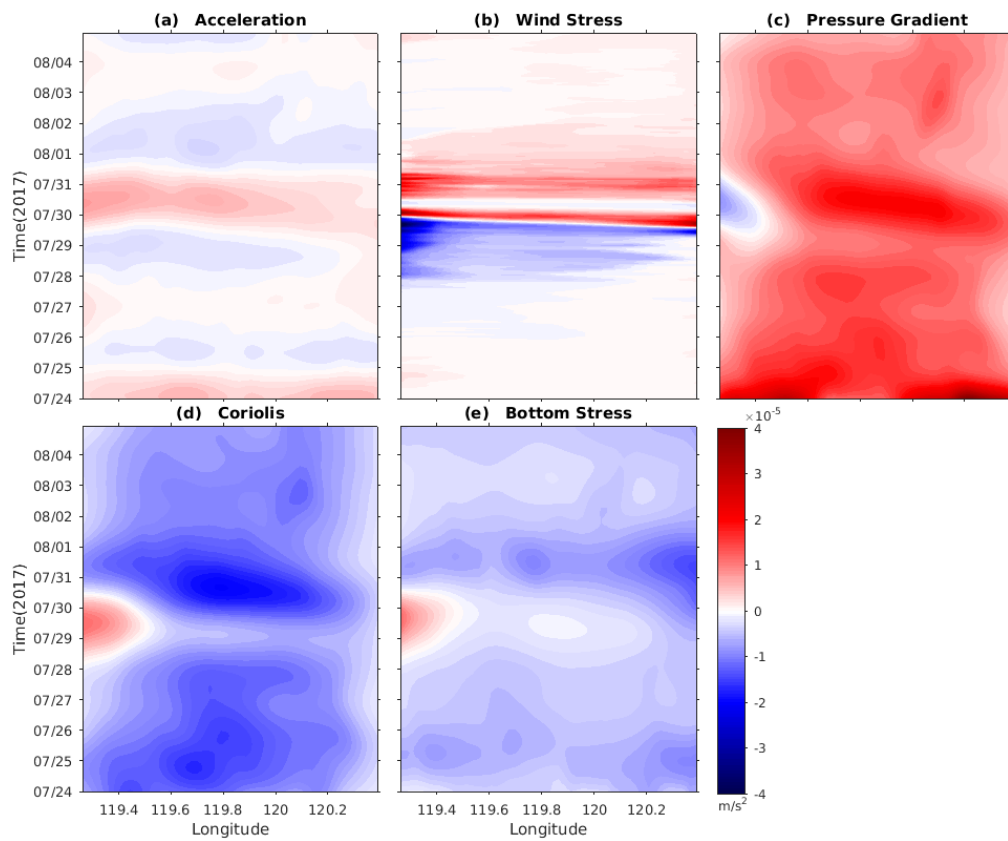


**Figure 12.** Diagrams of hourly ROMS output of depth-averaged along-shore momentum balance terms (Equation (4)) extracted from the cross-shore section shown in Figure 8f. Extracted variables include (a) acceleration, (b) wind stress, (c) pressure gradient, (d) Coriolis, and (e) bottom stress. Positive is in the along-shore directions.

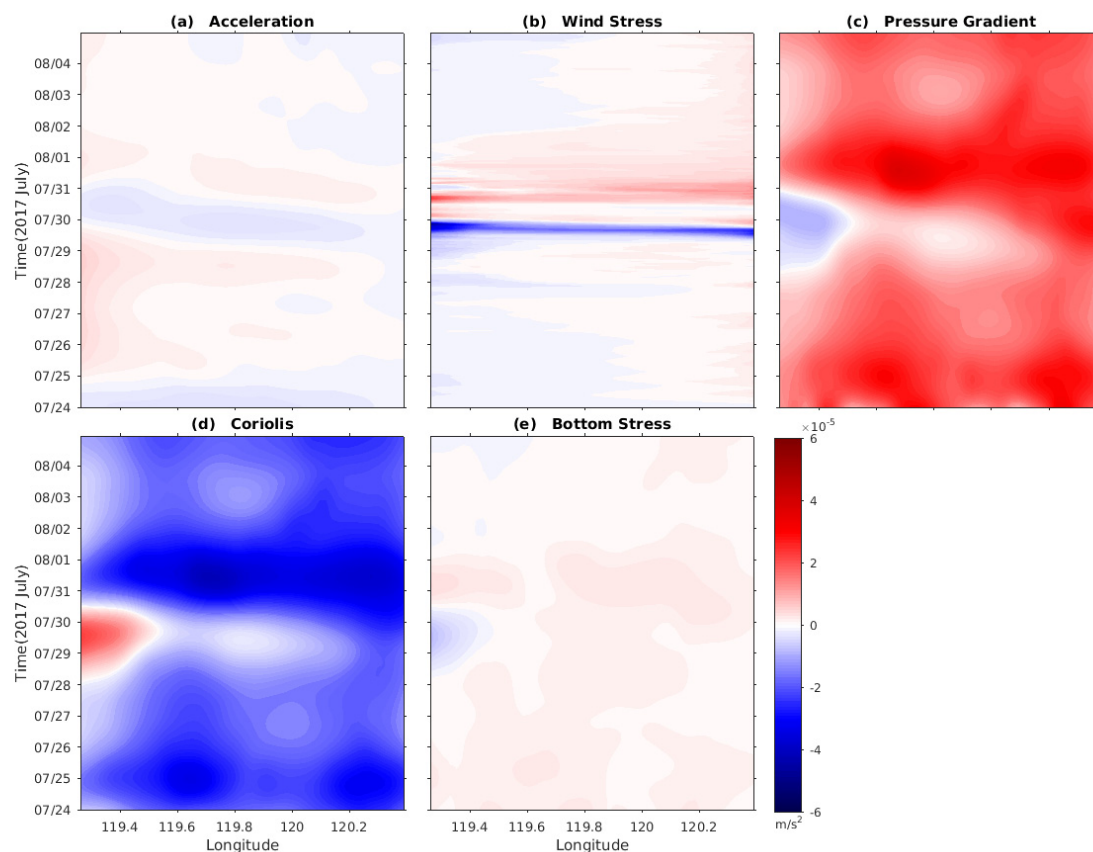


**Figure 13.** Diagrams of hourly ROMS output of the depth-averaged cross-shore momentum balance terms (Equation (5)) extracted from the cross-shore section shown in Figure 9f. Extracted variables include (a) acceleration, (b) wind stress, (c) pressure gradient, (d) Coriolis, and (e) bottom stress. Positive is in the onshore directions.

## 5. Summary

### 5.1. Main Findings

The hydrodynamic response of coastal water in the Taiwan Strait to Typhoon Nesat (2017) was investigated based on simulations using a fully-coupled atmosphere-ocean-wave model, COAWST.

The model results agree with observations for the intensity and track of Typhoon Nesat, sea level air pressure and wind speed from the WRF model, as well as tidal characteristics and significant wave heights from the SWAN model, indicating that the coupled modelling system accurately reproduced the main features of atmospheric and oceanic motions under the storm.

Ocean surface currents response were characterised by a pattern consistent with the classic Ekman theory, e.g., surface flow at a  $45^\circ$  angle to the right of the wind, which is supported by previous observational studies (e.g., [29]). Prior to the storm, the strait was dominated by barotropic tidal currents, whereas both barotropic and baroclinic flow components for the entire water column were impacted by passage of the typhoon.

For volume transport crossing the TWS, when the storm was approaching, the north-eastward volume transport was significantly reduced or even temporally reversed, following the variations in the along-shore wind stress. At landfall near the coast of Fujian Province, the winds were from north-east and notably intensified, which resulted in the quick restoration of north-eastward volume transport back to its pre-storm intensity. The response of ocean current and volume transport indicates that the dynamic features in the TWS can be significantly influenced by a typhoon with an intensity of only category one like Nesat (2017).

The coastal regions of Fujian Province (the west side of the TWS) experienced the maximum storm surge, while the east side of TWS exhibited only moderate storm surge. Surface heat flux, vertical diffusion, and advection all played a role in changing the water temperature in the upper 30 m water column whereas only advection determined the water temperature in the lower water column during the storm. In the along-shore direction, acceleration was largely determined by a combined effect of surface wind stress and bottom stress; in the cross-shore direction, the dominant terms were pressure gradient and Coriolis acceleration, indicating that the effect of storm on the geostrophic balance was small.

## 5.2. Future Works

Due to the fact that the magnitude of simulated pre-storm volume transport across the TWS is in agreement with previous observational studies [17,83], and the simulated typhoon track and intensity are generally consistent with observations, the simulated changes in volume transport are presumably to be truly induced by typhoon Nesat. However, more observational data should be used, and more case studies need to be carried out to further verify model.

The local intensification of storm surge found in coastal regions directly in right front of Nesat's landing point based on our model results is very similar to the other case study of [85]. The features of storm surge are determined by topography and atmospheric conditions. Several mechanisms have been proposed to explain why the localized storm surge can be generated by a storm, including a surface current created by the friction of storm wind exerting on sea surface, pressure-induced surge, and Seiche oscillation due to steep bathymetry [85]. Estimating the contribution of each component is vital to understanding of the local features of storm surge, which is also an interesting topic of study for the future.

Wave Extremes (e.g., [86]) generated by a typhoon are of particular importance to marine structure. Using coupled model combined observational data from buoys to investigate their evolution is also an important research work in the future. Additionally, the impact of cyclones on the evolution of the coastal strip and sediment dynamics (e.g., [87]) are also worth studying.

Furthermore, our previous works (e.g., [2,50,88–93]) indicate that oceanic thermohaline and dynamic features play an important role in upper ocean response to a single or sequential typhoons based on multiple observation data and model simulations. However, these works were mainly in the marginal sea (the South China Sea) and we may further follow the study of this paper, and study how some special topographic features such as with many islands or straits influences the structure of the oceanic response to typhoons in the future.

**Author Contributions:** R.W. designed the experiments and wrote the original manuscript; H.Z. improved the manuscript; R.W., Q.Y., D.T., B.H., S.W. and H.Z. contributed to the analysis of the data and discussion of the results.

**Funding:** This study was supported by the National Key R&D Project of China (2018YFC1506403, 2017YFC1404201), the Fundamental Research Funds for the Central Universities (No. 19lgzd07), the National Natural Science Foundation of China (41806021, 41621064, 41874046, 41705048, 41730535), the Scientific Research Fund of the Second Institute of Oceanography, MNR (JG1813), the National Program on Global Change and Air-Sea Interaction (GASI-IPOVAI-04) and the China Ocean Mineral Resources Research and Development Association Program (DY135-E2-3-01).

**Acknowledgments:** We thank two anonymous reviewers and the editor for their insightful comments and suggestions. All data used in this paper are open source as described in Section 2. The authors express sincere gratitude to the data providers.

**Conflicts of Interest:** The authors declare no conflicts of interest. The funding sponsors had no role in the design of the study; in the collection, analyses, or interpretation of data; in the writing of the manuscript, and in the decision to publish the results.

## References

1. Yin, X.; Wang, Z.; Liu, Y.; Xu, Y. Ocean response to Typhoon Ketsana traveling over the northwest Pacific and a numerical model approach. *Geophys. Res. Lett.* **2007**, *34*, L21606. [[CrossRef](#)]
2. Zhang, H.; Chen, D.; Zhou, L.; Liu, X.; Ding, T.; Zhou, B. Upper ocean response to typhoon Kalmaegi (2014). *J. Geophys. Res. Oceans* **2016**, *121*, 6520–6535. [[CrossRef](#)]
3. Song, D.; Guo, L.; Duan, Z.; Xiang, L. Impact of Major Typhoons in 2016 on Sea Surface Features in the Northwestern Pacific. *Water* **2018**, *10*, 1326. [[CrossRef](#)]
4. Liu, J.; Cai, S.; Wang, S. Observations of strong near-bottom current after the passage of Typhoon Pabuk in the South China Sea. *J. Mar. Syst.* **2011**, *87*, 102–108. [[CrossRef](#)]
5. Liu, J.; He, Y.; Li, J.; Cai, S.; Wang, D.; Huang, Y. Cases study of nonlinear interaction between near-inertial waves induced by typhoon and diurnal tides near the Xisha Islands. *J. Geophys. Res. Oceans* **2018**, *123*, 2768–2784. [[CrossRef](#)]
6. Zhao, H.; Han, G.; Zhang, S.; Wang, D. Two phytoplankton blooms near Luzon Strait generated by lingering Typhoon Parma. *J. Geophys. Res. Biogeosci.* **2013**, *118*, 412–421. [[CrossRef](#)]
7. Zhao, H.; Wang, Y. Phytoplankton increases induced by tropical cyclones in the South China Sea during 1998–2015. *J. Geophys. Res. Oceans* **2018**, *123*, 2903–2920. [[CrossRef](#)]
8. Glenn, S.M.; Miles, T.N.; Seroka, G.N.; Xu, Y.; Forney, R.K.; Yu, F.; Roarty, H.; Schofield, O.; Kohut, J. Stratified coastal ocean interactions with tropical cyclones. *Nat. Commun.* **2016**, *7*, 10887. [[CrossRef](#)]
9. Seroka, G.; Miles, T.; Xu, Y.; Kohut, J.; Schofield, O.; Glenn, S. Rapid shelf-wide cooling response of a stratified coastal ocean to hurricanes. *J. Geophys. Res. Oceans* **2017**, *122*, 4845–4867. [[CrossRef](#)]
10. Ding, W. The characteristics of the tides and tidal currents in the Taiwan Strait. *J. Oceanogr. Taiwan Strait* **1983**, *2*, 1–8.
11. Fang, G.; Yang, J.; Thao, Y. A two-dimensional numerical model for tidal motion in the Taiwan Strait. *Mar. Geophys. Res.* **1984**, *7*, 267–276. [[CrossRef](#)]
12. Fang, G. Tide and tidal current charts for the marginal seas adjacent to China. *Chin. J. Oceanol. Limnol.* **1986**, *4*, 1–16.
13. Fang, G.; Kwok, Y.K.; Yu, K.; Zhu, Y. Numerical simulation of principal tidal constituents in the South China sea, Gulf of Tonkin and Gulf of Thailand. *Cont. Shelf Res.* **1999**, *19*, 845–869. [[CrossRef](#)]
14. Yu, H.Q.; Yu, H.M.; Wang, L.; Kuang, L.; Wang, H.; Ding, Y.; Ito, S.; Lawen, J. Tidal propagation and dissipation in the Taiwan Strait. *Cont. Shelf Res.* **2017**, *136*, 57–73. [[CrossRef](#)]
15. Fu, Z.; Hu, J.; Yu, G. Seawater flux through Taiwan Strait. *Chin. J. Oceanol. Limnol.* **1991**, *9*, 232–239.
16. Fang, G.; Zhao, B.; Zhu, Y. Water volume transport through the Taiwan Strait and the continental shelf of the East China Sea measured with current meters. In *Oceanography of Asian Marginal Seas*; Takano, K., Ed.; Elsevier: New York, NY, USA, 1991; pp. 345–358.
17. Wang, Y.H.; Jan, S.; Wang, D.P. Transport and tidal current estimates in the Taiwan Strait from shipboard ADCP observations (1999–2001). *Estuar. Coast. Shelf Sci.* **2003**, *57*, 193–199. [[CrossRef](#)]
18. Wu, C.R.; Chao, S.Y.; Hsu, C. Transient, seasonal and interannual variability of the Taiwan Strait Current. *J. Oceanogr.* **2007**, *63*, 821–833. [[CrossRef](#)]
19. Yang, J. An oceanic current against the wind: How does Taiwan Island steer warm water into the East China Sea? *J. Phys. Oceanogr.* **2007**, *37*, 2563–2569. [[CrossRef](#)]
20. Zhang, W.Z.; Hong, H.S.; Yan, X.H. Typhoons enhancing northward transport through the Taiwan Strait. *Cont. Shelf Res.* **2013**, *56*, 13–25. [[CrossRef](#)]
21. Chang, Y.L.; Miyazawa, Y.; Guo, X. Effect of mesoscale eddies on the Taiwan Strait current. *J. Phys. Oceanogr.* **2015**, *45*, 1651–1666. [[CrossRef](#)]
22. Jan, S.; Wang, J.; Chern, C.S.; Chao, S.Y. Seasonal variation of the circulation in the Taiwan Strait. *J. Mar. Syst.* **2002**, *35*, 249–268. [[CrossRef](#)]
23. Li, C.; Hu, J.; Jan, S.; Wei, Z.; Fang, G.; Zheng, Q. Winter-spring Fronts in Taiwan Strait. *J. Geophys. Res. Oceans* **2006**, *111*. [[CrossRef](#)]
24. Hu, J.Y.; Kawamura, H.; Li, C.Y.; Hong, H.S.; Jiang, Y.W. Review on current and seawater volume transport through the Taiwan Strait. *J. Oceanogr.* **2010**, *66*, 591–610. [[CrossRef](#)]

25. Feng, X.; Li, M.; Yin, B.; Yang, D.; Yang, H. Study of storm surge trends in typhoon prone coastal areas based on observations and surge-wave coupled simulations. *Int. J. Appl. Earth Obs. Geoinf.* **2018**, *68*, 272–278. [[CrossRef](#)]
26. Liu, W.C.; Huang, W.C.; Chen, W.B. Modeling the interaction between tides and storm surges for the Taiwan coast. *Environ. Fluid Mech.* **2016**, *16*, 721–745. [[CrossRef](#)]
27. Yu, X.; Pan, W.; Zheng, X.; Zhou, S.; Tao, X. Effects of wave-current interaction on storm surge in the Taiwan strait: Insights from typhoon Morakot. *Cont. Shelf Res.* **2017**, *146*, 47–57. [[CrossRef](#)]
28. Wang, A.J.; Ye, X.; Du, X.; Zheng, B. Observations of cohesive sediment behaviors in the muddy area of the northern Taiwan Strait, China. *Cont. Shelf Res.* **2014**, *90*, 60–69. [[CrossRef](#)]
29. Chang, Y.C.; Tseng, R.S.; Centurioni, L.R. Typhoon induced strong surface flows in the Taiwan Strait and Pacific. *J. Oceanogr.* **2010**, *66*, 175–182. [[CrossRef](#)]
30. Shen, J.; Qiu, Y.; Zhang, S.; Kuang, F. Observation of Tropical Cyclone-Induced Shallow Water Currents in Taiwan Strait. *J. Geophys. Res. Oceans* **2017**, *122*, 5005–5021. [[CrossRef](#)]
31. Warner, J.C.; Armstrong, B.; He, R.; Zambon, J.B. Development of a coupled ocean-atmosphere-wave-sediment transport (COAWST) modeling system. *Ocean Model.* **2010**, *35*, 230–244. [[CrossRef](#)]
32. Remote Sensing Systems. Available online: <http://www.remss.com> (accessed on 20 September 2019).
33. GlobWave. Available online: <http://globwave.ifremer.fr/products/> (accessed on 20 September 2019).
34. Warner, J.C.; Perlin, N.; Skillingstad, E. Using the model coupling toolkit to couple earth system models. *Environ. Model. Softw.* **2008**, *23*, 1240–1249. [[CrossRef](#)]
35. Aldrian, E.; Sein, D.V.; Jacob, D.; Gates, L.D.; Podzun, R. Modeling Indonesian rainfall with a coupled regional model. *Clim. Dyn.* **2005**, *25*, 1–17. [[CrossRef](#)]
36. Chen, S.S.; Price, J.F.; Zhao, W.; Donelan, M.A.; Walsh, E.J. The CBLAST hurricane program and the next-generation fully coupled atmosphere-wave-ocean models for hurricane research and predictions. *Bull. Am. Meteorol. Soc.* **2007**, *88*, 311–317. [[CrossRef](#)]
37. O'Neill, L.W.; Chelton, D.B.; Esbensen, S.K. Observations of SST-induced perturbations of the wind stress field over the Southern Ocean on seasonal timescales. *J. Clim.* **2003**, *16*, 2340–2354. [[CrossRef](#)]
38. O'Neill, L.W.; Chelton, D.B.; Esbensen, S.K.; Wentz, F.J. High-resolution satellite measurements of the atmospheric boundary layer response to SST variations along the Agulhas Return Current. *J. Clim.* **2005**, *18*, 2706–2723. [[CrossRef](#)]
39. O'Neill, L.W.; Chelton, D.B.; Esbensen, S.K. The effects of SST-induced surface wind speed and direction gradients on Midlatitude Surface vorticity and divergence. *J. Clim.* **2010**, *23*, 255–281. [[CrossRef](#)]
40. Chelton, D.B.; Esbensen, S.K.; Schlax, M.G.; Thum, N.; Freilich, M.H.; Wentz, F.J.; Gentemann, C.L.; McPhaden, M.J.; Schopf, P.S. Observations of Coupling between Surface Wind Stress and Sea Surface Temperature in the Eastern Tropical Pacific. *J. Clim.* **2001**, *14*, 1479–1498. [[CrossRef](#)]
41. Chelton, D.B. The impact of SST specification on ECMWF surface wind stress fields in the eastern tropical Pacific. *J. Clim.* **2005**, *18*, 530–550. [[CrossRef](#)]
42. Chelton, D.B.; Schlax, M.G.; Samelson, R.M. Summertime Coupling between Sea Surface Temperature and Wind Stress in the California Current System. *J. Phys. Oceanogr.* **2007**, *37*, 495–517. [[CrossRef](#)]
43. Ocean-Modeling.Org. Available online: <http://www.myroms.org/> (accessed on 20 September 2019).
44. Shchepetkin, A.F.; McWilliams, J.C. The regional oceanic modeling system (ROMS): A split-explicit, free-surface, topography-following-coordinate oceanic model. *Ocean Model.* **2005**, *9*, 347–404. [[CrossRef](#)]
45. Skamarock, W.C.; Klemp, J.B.; Dudhia, J.; Gill, D.O.; Barker, D.M.; Duda, M.; Huang, X.Y.; Wang, W.; Powers, J.G. *A Description of the Advanced Research WRF Version 3*; NCAR Technical Note NCAR/TN-475+STR; National Center for Atmospheric Research: Boulder, CO, USA, 2008. [[CrossRef](#)]
46. Booij, N.; Ris, R.C.; Holthuijsen, L. A third-generation wave model for coastal regions 1. model description and validation. *J. Geophys. Res.* **1999**, *104*, 7649–7666. [[CrossRef](#)]
47. Zambon, J.B.; He, R.; Warner, J.C. Investigation of Hurricane Ivan using the coupled ocean-atmosphere-wave-sediment transport (COAWST) model. *Ocean Dyn.* **2014**, *64*, 1535–1554. [[CrossRef](#)]
48. Carniel, S.; Benetazzo, A.; Bonaldo, D.; Falcieri, F.; Miglietta, M.; Ricchi, A.; Sclavo, M. Scratching beneath the surface while coupling atmosphere, ocean and waves: Analysis of a dense water formation event. *Ocean Model.* **2016**, *101*, 101–112. [[CrossRef](#)]

49. Ricchi, A.; Miglietta, M.M.; Barbariol, F.; Benetazzo, A.; Bergamasco, A.; Bonaldo, D.; Cassardo, C.; Falcieri, F.M.; Modugno, G.; Russo, A.; et al. Sensitivity of a Mediterranean tropical-like cyclone to different model configurations and coupling strategies. *Atmosphere* **2017**, *8*, 92. [CrossRef]
50. Wu, R.; Zhang, H.; Chen, D.; Li, C.; Lin, J. Impact of Typhoon Kalmaegi (2014) on the South China Sea: Simulations using a fully coupled atmosphere-ocean-wave model. *Ocean Model.* **2018**, *131*, 132–152. [CrossRef]
51. Wu, Z.; Jiang, C.; Chen, J.; Long, Y.; Deng, B.; Liu, X. Three-Dimensional Temperature Field Change in the South China Sea during Typhoon Kai-Tak (1213) Based on a Fully Coupled Atmosphere–Wave–Ocean Model. *Water* **2019**, *11*, 140. [CrossRef]
52. Chen, J.; Jiang, C.; Wu, Z.; Long, Y.; Deng, B.; Liu, X. Numerical Investigation of Fresh and Salt Water Distribution in the Pearl River Estuary during a Typhoon Using a Fully Coupled Atmosphere-Wave-Ocean Model. *Water* **2019**, *11*, 646. [CrossRef]
53. Kain, J.S. The Kain-Fritsch convective parameterization: An update. *J. Appl. Meteorol. Clim.* **2004**, *43*, 170–181. [CrossRef]
54. Mlawer, E.; Taubman, S.; Brown, P.; Iacono, M.; Clough, S.A. Radiative transfer for inhomogeneous atmospheres: RRTM, a validated correlated-k model for the longwave. *J. Geophys. Res.* **1997**, *102*, 16663–16682. [CrossRef]
55. Dudhia, J. Numerical study of convection observed during the winter monsoon experiment using a mesoscale two-dimensional model. *J. Atmos. Sci.* **1989**, *46*, 3077–3107. [CrossRef]
56. Nakanishi, M.; Niino, H. An improved Mellor–Yamada level-3 model: Its numerical stability and application to a regional prediction of advecting fog. *Bound. Layer Meteorol.* **2006**, *119*, 397–407. [CrossRef]
57. Nakanishi, M.; Niino, H. Development of an improved turbulence closure model for the atmospheric boundary layer. *J. Meteorol. Soc. Jpn.* **2009**, *87*, 895–912. [CrossRef]
58. Cohen, A.E.; Cavallo, S.M.; Coniglio, M.C.; Brooks, H.E. A review of planetary boundary layer parameterization schemes and their sensitivity in simulating southeastern U.S. cold season severe weather environments. *Weather Forecast.* **2015**, *30*, 591–612. [CrossRef]
59. Janjić, Z.I. The step-mountain coordinate: Physical package. *Mon. Weather Rev.* **1990**, *118*, 1429–1443. [CrossRef]
60. Janjić, Z.I. The step-mountain eta coordinate model: Further developments of the convection, viscous sublayer, and turbulence closure schemes. *Mon. Weather Rev.* **1994**, *122*, 927–945. [CrossRef]
61. Janjic, Z.I. Non-Singular Implementation of the Mellor-Yamada Level 2.5 Scheme in the NCEP Meso Model. NCEP Office Note 61; 2002. Available online: <http://www.emc.ncep.noaa.gov/officenotes/newernotes/on437.pdf> (accessed on 6 November 2019).
62. Tewari, M.; Chen, F.; Wang, W.; Dudhia, J.; Lemone, M.A.; Mitchell, K.; Ek, M.; Gayno, G.; Wegiel, J.; Cuenca, R.H. Implementation and verification of the unified Noah land surface model in the WRF model. In Proceedings of the 20th Conference on Weather Analysis and Forecasting/16th Conference on Numerical Weather Prediction, Seattle, WA, USA, 14 January 2004; pp. 11–15.
63. Available online: <http://polar.ncep.noaa.gov/pub/history/sst> (accessed on 20 September 2019).
64. Taylor, P.K.; Yelland, M.J. The dependence of sea surface roughness on the height and steepness of the waves. *J. Phys. Oceanogr.* **2001**, *31*, 572–590. [CrossRef]
65. National Center for Atmospheric Research. Available online: <http://rda.ucar.edu/datasets/ds083.2/> (accessed on 20 September 2019).
66. von Storch, H.; Langenberg, H.; Feser, F. A spectral nudging technique for spectral downscaling purposes. *Mon. Weather Rev.* **2000**, *128*, 3664–3673. [CrossRef]
67. General Bathymetric Chart of the Oceans. Available online: <https://www.gebco.net> (accessed on 20 September 2019).
68. Penven, P.; Marchesiello, P.; Debreu, L.; Lefèvre, J. Software tools for pre-and post processing of oceanic regional simulations. *Environ. Model. Softw.* **2008**, *23*, 660–662. [CrossRef]
69. Bracco, A.; Choi, J.; Joshi, K.; Hao, L.; McWilliams, J.C. Submesoscale currents in the northern Gulf of Mexico: Deep phenomena and dispersion over the continental slope. *Ocean Model.* **2016**, *101*, 43–58. [CrossRef]
70. HYCOM Consortium for Data Assimilative Modeling. Available online: <https://hycom.org/data/glb0pt08/expt-91pt1> (accessed on 20 September 2019).
71. Available online: <http://volkov.oce.orst.edu/tides/global.html> (accessed on 6 November 2019).

72. Warner, J.; Sherwood, C.; Arango, H.; Signell, R. Performance of four turbulence closure models implemented using a generic length scale method. *Ocean Model.* **2005**, *8*, 81–113. [[CrossRef](#)]
73. Kumar, N.; Voulgaris, G.; Warner, J.C.; Olabarrieta, M. Implementation of the vortex force formalism in the coupled ocean-atmosphere-wave-sediment transport (COAWST) modeling system for inner shelf and surf zone applications. *Ocean Model.* **2012**, *47*, 65–95. [[CrossRef](#)]
74. Index. Available online: <http://polar.ncep.noaa.gov/pub/history/waves/> (accessed on 20 September 2019).
75. Kirby, J.T.; Chen, T.M. Surface waves on vertically sheared flows: Approximate dispersion relations. *J. Geophys. Res.* **1989**, *94*, 1013–1027. [[CrossRef](#)]
76. Komen, G.J.; Hasselmann, S.; Hasselmann, K. On the existence of a fully developed wind-sea spectrum. *J. Phys. Oceanogr.* **1984**, *14*, 1271–1285. [[CrossRef](#)]
77. Galarneau, T.J., Jr.; Davis, C.A. Diagnosing forecast errors in tropical cyclone motion. *Mon. Weather Rev.* **2013**, *141*, 405–430. [[CrossRef](#)]
78. Marks, F.; Shay, L.K. Landfalling tropical cyclones: Forecast problems and associated research opportunities: Report of the 5th prospectus development team to the US weather research program. *Bull. Am. Meteorol. Soc.* **1998**, *79*, 305–323.
79. Cha, D.; Jin, C.; Lee, D.; Kuo, Y. Impact of intermittent spectral nudging on regional climate simulation using weather research and forecasting model. *J. Geophys. Res. Atmos.* **2011**, *116*, 10103. [[CrossRef](#)]
80. Hu, C.K.; Chiu, C.T.; Chen, S.H.; Kuo, J.Y.; Jan, S.; Tseng, Y.H. Numerical simulation of barotropic tides around Taiwan. *Terr. Atmos. Ocean. Sci.* **2010**, *21*, 71–84. [[CrossRef](#)]
81. Atlas of the Oceans Editorial Board (Ed.) *Marine Atlas of the Bohai Sea, Yellow Sea and East China Sea*; (Hydrological); The Ocean Press: Beijing, China, 1993. (In Chinese)
82. Olabarrieta, M.; Warner, J.C.; Armstrong, B.; Zambon, J.B.; He, R. Ocean-atmosphere dynamics during Hurricane Ida and Nor'Ida: An application of the coupled ocean-atmosphere-wave-sediment transport (COAWST) modeling system. *Ocean Model.* **2012**, *43–44*, 112–137. [[CrossRef](#)]
83. Jan, S.; Sheu, D.D.; Kuo, H.M. Water mass and throughflow transport variability in the Taiwan Strait. *J. Geophys. Res. Oceans* **2006**, *111*, C12012. [[CrossRef](#)]
84. Wikipedia. Available online: [https://en.wikipedia.org/wiki/Typhoon\\_Haitang](https://en.wikipedia.org/wiki/Typhoon_Haitang) (accessed on 20 September 2019).
85. Mori, N.; Kato, M.; Kim, S.; Mase, H.; Shibutani, Y.; Takemi, T.; Tsuboki, K.; Yasuda, T. Local amplification of storm surge by Super Typhoon Haiyan in Leyte Gulf. *Geophys. Res. Lett.* **2014**, *41*, 5106–5113. [[CrossRef](#)]
86. Barbariol, F.; Alves, J.H.; Benetazzo, A.; Bergamasco, F.; Bertotti, L.; Carniel, S.; Cavaleri, L.; Chao, Y.Y.; Chawla, A.; Ricchi, A.; et al. Numerical modeling of space-time wave extremes using WAVEWATCH III. *Ocean Dyn.* **2017**, *67*, 535. [[CrossRef](#)]
87. Bonaldo, D.; Antonioli, F.; Archetti, R.; Bezzi, A.; Correggiari, A.; Davolio, S.; De Falco, G.; Fantini, M.; Fontolan, G.; Furlani, S.; et al. Integrating multidisciplinary instruments for assessing coastal vulnerability to erosion and sea level rise: Lessons and challenges from the Adriatic Sea, Italy. *J. Coast. Conserv.* **2019**, *23*, 19. [[CrossRef](#)]
88. Zhang, H.; Wu, R.; Chen, D.; Liu, X.; He, H.; Tang, Y.; Ke, D.; Shen, Z.; Li, J.; Xie, J.; et al. Net Modulation of Upper Ocean Thermal Structure by Typhoon Kalmaegi (2014). *J. Geophys. Res. Oceans* **2018**, *123*, 7154–7171. [[CrossRef](#)]
89. Zhang, H.; Liu, X.; Wu, R.; Liu, F.; Yu, L.; Shang, X.; Qi, Y.; Wang, Y.; Song, X.; Xie, X.; et al. Ocean Response to Successive Typhoons Sarika and Haima (2016) Based on Data Acquired via Multiple Satellites and Moored Array. *Remote Sens.* **2019**, *11*, 2360. [[CrossRef](#)]
90. Wu, R.; Li, C. Upper ocean response to the passage of two sequential typhoons. *Deep Sea Res. Part I Oceanogr. Res. Pap.* **2018**, *132*, 68–79. [[CrossRef](#)]
91. Ning, J.; Xu, Q.; Feng, T.; Zhang, H.; Wang, T. Upper Ocean Response to Two Sequential Tropical Cyclones over the Northwestern Pacific Ocean. *Remote Sens.* **2019**, *11*, 2431. [[CrossRef](#)]

92. Ning, J.; Xu, Q.; Zhang, H.; Wang, T.; Fan, K. Impact of Cyclonic Ocean Eddies on Upper Ocean Thermodynamic Response to Typhoon Soudelor. *Remote Sens.* **2019**, *11*, 938. [[CrossRef](#)]
93. Yue, X.; Zhang, B.; Liu, G.; Li, X.; Zhang, H.; He, Y. Upper Ocean Response to Typhoon Kalmaegi and Sarika in the South China Sea from Multiple-Satellite Observations and Numerical Simulations. *Remote Sens.* **2018**, *10*, 348. [[CrossRef](#)]



© 2019 by the authors. Licensee MDPI, Basel, Switzerland. This article is an open access article distributed under the terms and conditions of the Creative Commons Attribution (CC BY) license (<http://creativecommons.org/licenses/by/4.0/>).